RSC Advances

ROYAL SOCIETY OF CHEMISTRY

www.rsc.org/advances

ARTICLE TYPE www. rsc.org/xxxxxx | XXXXXXXX

Spin-dependent transport properties of a chromium porphyrin-based molecular embedded between two graphene nanoribbon electrodes†

Tong Chen,[a] Lingling Wang,*[a] Xiaofei Li,*[b] Kaiwu Luo,[a] Liang Xu,[a] Quan Li,[a] Xianghua Zhang[a,c] and Mengqiu Long [d]

Received Xth XXXXXXXXXX 20XX, Accepted Xth XXXXXXXXX 20XX
First published on the web Xth XXXXXXXXXX 200X
DOI: 10.1039/b000000x

By using the nonequilibrium Green's function formalism combined with the density-functional theory, we present a theoretical study of the spin-dependent electron transport of a molecular device constructed by a chromium porphyrin molecule linking with two carbon chains sandwiched between two semi-infinite zigzag-edged graphene nanoribbon(ZGNR) electrodes, where the ZGNRs are modulated by external magnetic field. The results show that the single spin-conducting can be obtained by performing different magnetic configuration of the leads. The coexistence of spin-filtering with 100% spin-polarization, rectifying and negative differential resistance(NDR) behaviors in our model device is demonstrated and the mechanisms are proposed for these phenomena.

1 INTRODUCTION

The electron transport properties of molecular-scale device have been researched extensively for the decades [1–3]. Particularly, the molecular spintronics in controlling and manipulating the electron transport properties of spins at the organic single-molecule level obtained much attentions [4–7]. It is known that many particular spin-related phenomena, like spin-filtering [8–12], rectification [13,14], spin-valve [15,16], spin crossover [17], Kondo effect [18] and spin negative differential resistance(NDR) phenomena [19–21] can be found in molecular spintronic devices, which can make molecular spintronics a very promising material in next-generation electronics devices.

Among many potential molecular candidates, porphyrin derivatives form a good candidate for molecular electronic devices. Since their electronic and magnetic properties can be effectively modulated by the central transition metal or ligands, the special properties of porphyrin derivatives have been investigated by both theorists and experimentalist [22–26]. For example, Chen et al. reported that a ligated iron atom can be used as a switching device, which has a considerable spin-polarization in current [26]. Cho et al. predicted a half-metallic spintronic device in a one-dimensional chromium porphyrin array capped between two Au electrodes [23]. Zeng et al. found the interesting spin filtering and magnetoresistance effects in a spintronic device constructed by two manganese porphyrin molecules connected with a p-phenylene-ethynylene group [25].

Because of the successful fabrication of graphene and graphene nanoribbon(GNR) [27,28], which are usually proposed as electrode in spintronics devices. When in contrast to traditional metal electrodes, GNR are better performed by their unique physical properties, such as high carrier mobility, magnetic edge effects and the atomistic size [29–32]. Two typical types of GNRs can be obtained by tailing a graphene sheet along a straight line: zigzag- and armchair-edge GNRs(ZGNRs and AGNRs), and edge states in ZGNRs are spin-polarized with an anti-ferromagnetic(AFM) ground state, whereas hydrogen-terminated armchair GNRs (aGNRs) do not exhibit such edge-localized states and are not spin-polarized. In addition, the single carbon atomic chain, which can be carved out from a graphene sheet by using a high-energy electron beam, plays an important role in molecular devices [33–36]. At the same time the carbon-atomic chains as spin-transmitters have triggered tremendous interests. For example, Zeng et al. found a perfect spin filters and spin valves with a large bias-dependent magnetoresistance in carbon-chain-bridging between two GNR leads [37]. Although it's possible to fabricate a molecular device connecting with graphene nanogap electrodes [38], the carbon-chain capped with organic molecular sandwiched between two GNR leads have rarely been reported. As the monomeric chromium porphyrin can be synthesized in experiment [39,40], and Cho et al demonstrated that among other transition metal ions, chromium porphyrin

[a] *School of Physics and Microelectronic Science, Hunan University and Key Laboratory for Micro-Nano Physics and Technology of Hunan Province, Changsha 410082, China.*
[b] *School of Optoelectronic Information, University of Electronic Science and Technology of China, Chengdu, Sichuan, 610054, P.R. China.*
[c] *Department of Electrical and Information Engineering, Hunan Institute of Engineering, Xiangtan 411101, P.R. China.*
[d] *School of Physics and Electronics, Institute of Super Microstructure and Ultrafast Process, Central South University, Changsha 410083, China.*

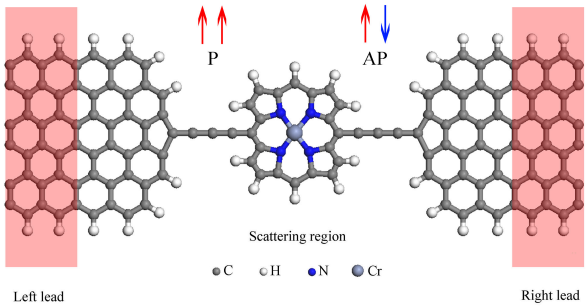

Fig. 1 Schematic of the model device with a coplanar configuration between plane of chromium porphyrin molecular and two zigzag graphene nanoribbon leads. The shaded areas indicate the leads with two repeated carbon unit cells along the transport direction(z), which are modulated by an external magnetic field along the +y or -y direction, respectively.

molecular turned out be the best choice for designing a new spin filter device[23], we investigated the spin-resolved transport characteristics of a chromium porphyrin molecular-based spintronics molecular devices.

In this paper, we investigated the spin-resolved electron transport properties of a molecular spintronics in which two carbon chains capping with a chromium porphyrin molecular sandwiched between two ZGNR electrodes. Although the ZGNRs are magnetic with an anti-ferromagnetic(AFM) ground state, it can be switched to a more stable ferromagnetic(FM) state when applied an external transverse electronic field or magnetic field[41,42]. And we can set the magnetization configuration of the leads as parallel configuration(P, the magnetic fields of two leads in the same y direction) or antiparallel configuration(AP, the magnetic fields of the left and the right leads are in the opposite direction corresponding to the +y or -y direction, which can be easily performed in experiment). As a result, the multifunctional spintronic devices with a single spin-conducting, perfect spin-filtering with 100% spin-polarity, spin-rectifying and NDR characteristics can be obtained by controlling the magnetic orientations of the two electrodes, which has significant application in future high-performance multifunctional atomic-scale spintronic device.

2 MODELS and Methods

The molecular device is illustrated in Fig. 1, where the chromium porphyrin molecular connected with two carbon atomic chains is covalently bridged between two ZGNR electrodes. The number of six zigzag lines are chosen along the width as an even number zigzag lines can exhibit a dual spin-

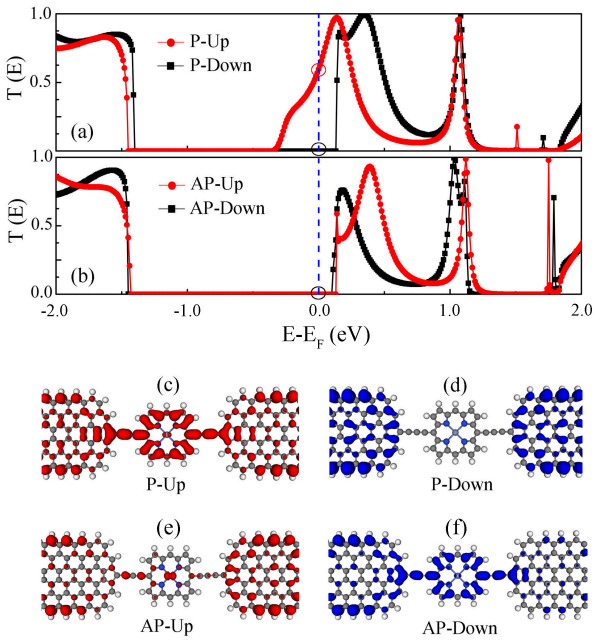

Fig. 2 The spin-dependent electron transmission spectra at zero bias in (a) P and (b) AP spin configurations. (c)-(d) and (e)-(f) are the spin-resolved LDOS at the Fermi level of P and AP spin configurations, respectively. The isovalues of spin-resolved LDOS are 0.004 a.u.

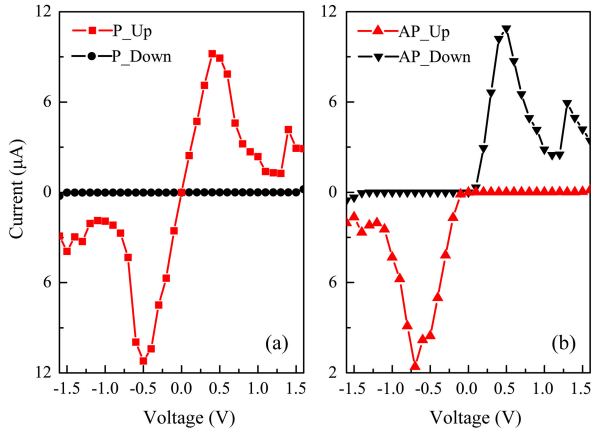

Fig. 3 Calculated current as a function of the applied bias for (a) P and (b) AP spin configurations.

filtering effect in the symmetrical ZGNRs[43]. The device can be divided into three regions: the left electrode, the scattering region and the right electrode. And the semi-infinite leads are described by two repeated carbon unit cells. The enough surface layers are essentially adopted to properly screen the perturbation effect from the central region. Just following previous researches, we connected the carbon atomic chain with the ZGNR leads through a five-membered carbon rings and all the edge dangling bonds passivated with hydrogen atoms[9,37].

The geometric optimization and spin-resovled electron transport properties were calculated by performing the first-principle software package Atomistix ToolKit(ATK)[44], which is based on the spin-polarized density-functional theory(DFT) in combination with the nonequilibrium Greens function-s(NEGF). The electron exchange-correlation potential use generalized gradient approximation(GGA) in the Perdew-Burke-Ernzerhof(PBE) form[45]. A single-polarized basis is set for carbon atoms and the double-polarized is set for other atoms. In our calculation, the Brillouin zone (BZ) is sampled by $1 \times 1 \times 100$ Monkhorst-Pack k-mesh. In order to achieve the balance between calculation efficiency and accuracy, the grid integration of cutoff energy is defined by 150 Ry and the maximum force tolerance is 0.01 eV/Å. The vacuum layer is used at least 15 Å to avoid the spurious interaction between periodic images. The nonliner current through the center s-cattering region as a function of applied external bias can be calculated using the Landauer formula[33,46]:

$I^{\uparrow(\downarrow)} = \frac{e}{\hbar}\int_{-\infty}^{\infty}\{T^{\uparrow(\downarrow)}(E)[f_L(E,\mu)\text{-}f_R(E,\mu)]\}dE$,

where $\int_{L(R)}(E,\mu)$ is the equilibrium Fermi distribution for the left (or the right) electrode, and $\mu_{L(R)}$=E_F±eV/2 is the electrochemical potential of the left and right electrodes in terms of the common Fermi energy E_F, and $T^{\uparrow(\downarrow)}(E)$ is the spin-resolved transmission defined as

$T^{\uparrow(\downarrow)}(E)$=T$\gamma$[$\Gamma_L G^R \Gamma_R G^A$]$^{\uparrow(\downarrow)}$,

where $G^{R(A)}$ is the retarded (or the advanced) Greens function of the central region and $\Gamma_{L(R)}$ is the coupling matrix of the left (or the right) electrode.

3 Result and discussion

The spin-resolved electron transmission spectra of P and AP spin configurations were calculated and plotted in Fig. 2(a) and 2(b), respectively. It is clearly that in both spin configurations, the transmission spectra are spin-split. One can see from Fig. 2(a) that the spin-up spectrum presents a broad and strong peak around the E_F in P configuration which means the spin-up electrons can easily pass through the device, while the peak moves right side into the higher energy region with transmission spectra at the E_F being suppressed in the AP configuration, as shown in Fig. 2(b). However, the positions of spin-down transmission spectra have changed slightly when the spin configuration transforms from P configuration to AP

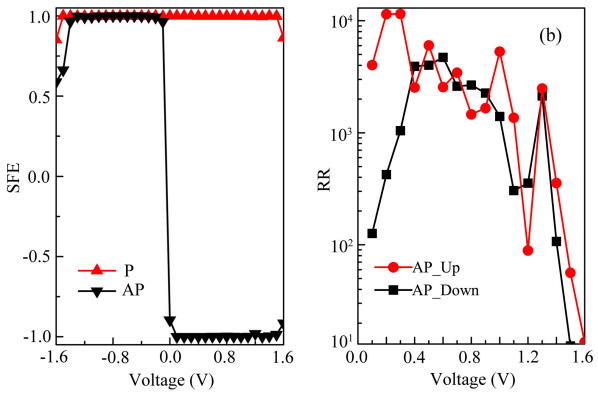

Fig. 4 (a) The calculated spin filtering efficiency(SFE) curves for P and AP spin configurations. (b) The rectification ratio curves for spin-up and spin-down electrons of the AP spin configuration.

configuration, except for the magnitude of spin-down peaks around the E_F in P configuration are generally larger than that in AP configuration. What's more, the spin-down currents are blocked at the E_F both in P and AP configurations. The asymmetrical spin-down and spin-up currents indicate the occurrence of spin-polarization both in P and AP configurations. The spin polarization can be understood by presenting the spin-resolved local density of states(LDOS) at the E_F. Figs. 2(c) and 2(d) show the spin-up and spin-down LDOS at the E_F in P configuration, respectively. The spin-up electrons can easily across the central scattering region from right to left and a excellent coupling can be found on the chromium porphyrin molecular which means the molecular provided good channels for transmission. However, the LDOS of spin-down are completely blocked on the chromium porphyrin molecular, which means no channel can be provided for transport of spin-down electrons. Hence, the 100% spin-polarization at the E_F can be obtained at zero bias indicating a perfect spin-filtering. While for AP configuration, the spin polarization occurs s-maller than in P configuration with both the spin transmission channels being blocked around the E_F at zero bias. One can see the spin-resolved LDOS distribution of AP configuration, the spin-up LDOS is weak on the chromium porphyrin molecular in Fig. 2(e) and the spin-down one is suppressed on the right side of the device in Figs. 2(f). This is why the spin-polarization of P configuration is larger than AP configuration.

We calculated spin polarized currents as a function of the applied external bias for P and AP spin configurations in Figs. 3(a) and 3(b), respectively. The distinct features of single spin-conducting and spin-NDR effects can be found: For the P configuration, the spin-up and spin-down currents seem symmetrical at the same magnitude of positive and negative bias. One can see that when applied the positive bias, the spin-up current increases linearly at small biases and reaches its maximum

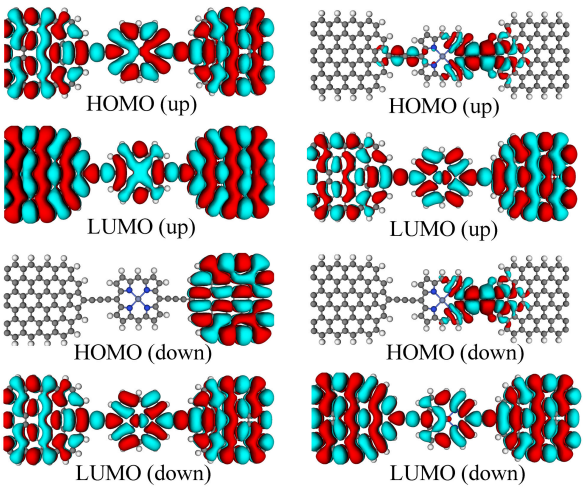

Fig. 5 Iso surfaces of MPSH orbitals for the P (left) and AP (right) configurations of chromium porphyrin-based molecular two probe systems at the zero bias, respectively. HOMO(Up), LUMO(Up), HOMO(Down) and LUMO(Down) represent the spin-up highest occupied molecular orbital, the spin-up lowest occupied molecular orbital, the spin-down highest occupied molecular orbital and the spin-down lowest unoccupied molecular orbital, respectively.

magnitude at V_b= 0.4 V(V_b= -0.5 V at the negative bias), while it decreases rapidly with further increasing the external bias, which indicates the onset of NDR phenomenon. However, the spin-down current is obviously much smaller than spin-up current. It is almost suppressed within the bias range from -1.6 to 1.6 V. Therefore, a perfect spin-filtering can be obtained in the P spin configuration. For the AP spin configuration, the spin-up current is similar as it in the P configuration at the negative bias while it is almost forbidden at the positive bias. One can see it increases dramatically at the very beginning and reaches its peak at the bias V_b= -0.7 V and then becomes weak with further increasing the bias, indicating the intrinsic NDR behavior. Nevertheless, the case of the spin-down current is just opposite to that of spin-up current in AP spin configuration. The spin-down electrons can easily pass through the device under positive bias and the peak of spin-down current appears at V_b= 0.5 V, but the spin-up current is almost suppressed at the bias range from 0.1 to 1.3 V. This finding means the device in AP configuration can be a dual spin filter or a dual spin diode, which is similar to that in the ZGNR device with a greatly improved performance[43]. We can reach a conclusion that the system can act as a single spin-conductor in P and AP configurations, and the interesting dual spin-diode is also found in AP configuration. As a result, the spin-NDR phenomena were found both in P and AP configurations. All these interesting phenomena indicate that our system hold great promising in high-speed device and multi-valued integration density of molecular circuits[47]. As the single spin-conducting in our designed device, we calculated and plotted the spin-filtering efficiency(SFE) of them, in Fig. 4(a). And we defined SFE = $(I_{up} - I_{down})/(I_{up} + I_{down})$. For the vanished current at the zero bias, we replaced it with the corresponding zero-bias transmission coefficients at the E_F of two spin configurations in Fig. 2. One can see that the SFE of P spin configuration is nearly 100% at the bias range from -1.5 to 1.5 V and it keeps nearly unchanged at high biases. While the SFE of AP configuration is much different to that in P spin configuration. The SFE keeps 100% at the negative bias from -0.2 to -1.3 V and then it reverses to -100% at the positive bias from 0.1 to 1.5 V. A perfect SFE behavior at such a wide bias range in P and AP configurations have significant practical application in spin devices. Additionally, the rectification ratio(RR) of spin-up and spin-down current in AP configuration are displayed in Fig. 4(b), the maximum rectifying ratio for spin-up

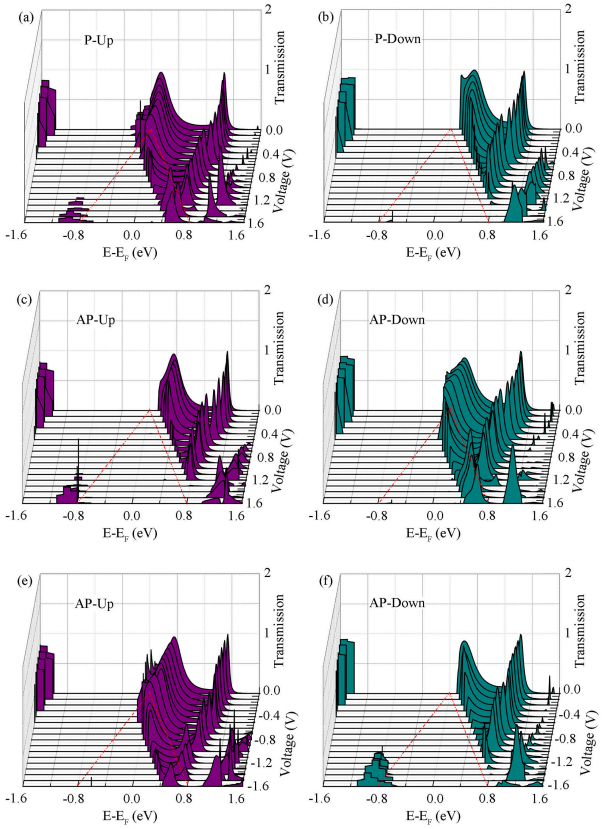

Fig. 6 (a) and (b) are the transmission spectra of spin-up and spin-down electrons in the P spin configuration at the bias range from 0.0 to 1.6 V. (c)-(f) are the transmission spectra of spin-up and spin-down in AP spin configuration at the bias of [0.0, 1.6]V, [0.0, 1.6]V, [0.0, -1.6]V, [0.0, -1.6]V, respectively. The red dashed lines denote the energy bias window.

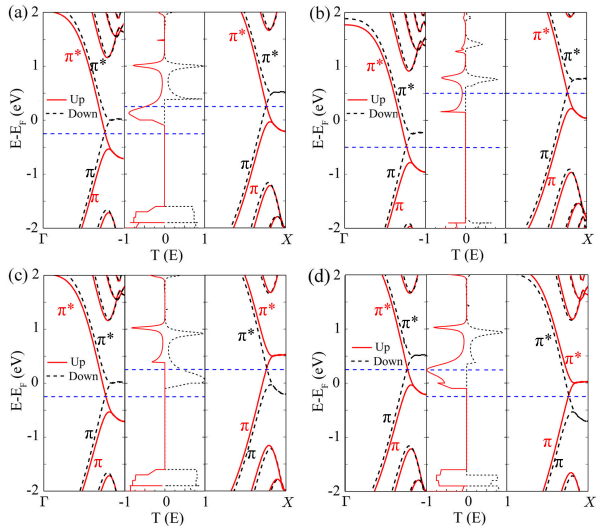

Fig. 7 The spin-resolved band structures for the left lead(left panels), transmission curve(middle panels), and band structure for the right lead(right panels). (a) and (b) represent the systems in P spin configuration at the bias of 0.5 and 1.0 V, respectively. (c) and (d) denote the system in AP spin configuration at ± 0.5 V, respectively. The horizontal blue dashed lines denote the chemical potentials of left and right electrodes.

current can reach 1.15×10^4 at the bias of 0.3 V, which is quite comparable to that of typical solid-state rectifier. Meantime, the rectifying behaviors can also be found in spin-down current with its maximum RR reaching to 4.7×10^3.

In order to illustrate the above interesting phenomena, we analyzed the distribution of the spin-poralized molecular projected self-consistent Hamitonian stats(MPSHs) of highest occupied molecular orbital (HOMO) and the lowest unoccupied molecular orbital (LUMO) in the cental scattering region at the zero bias in Fig. 5., respectively. As the molecular orbital can convey the charge carriers to participate in electron tunneling, the spatial distribution of frontier obitals can qualitatively illustrate the coupling between the scattering region and the electrodes. At the same time, only the greater delocalization of the MPSHs throughout the scattering region, the stronger transport peaks can be generated in the transmission spectrum. One can see from the left side of Fig. 5, the spin-up HOMO/LUMO in P are good delocalized, indicating the spin-up transmission peaks appear around the E_F, meanwhile the MPSH of spin-down LUMO separates as similar as the spin-up MPSHs, thus a spin-down transmission peak happens in the right side of the E_F. While the MPSH of spin-down HOMO localizes on the right part of the system corresponding to the small spin-down transmission at the left side of the E_F. And the distributions of spin-down HOMO/LUMO in AP configuration are the same as that in P configuration, which means the spin-down transmission efficiency just have changed slightly in P and AP configuration. However, the spin-up HOMO localizes on part of central region in AP configuration, so the spin-up transmission become small in the vicinity of the E_F, which indicates the HOMO transmission peaks are far from the Fermi level.

We also presented the spin-up and spin-down transmission spectra in P and AP configurations under different external bias in Fig. 6. As the spin-related currents are symmetrical both at positive and negative bias in P configuration, we only plotted the transmission spectra at the positive bias. As shown in Fig. 6(a), a strong and broad spin-up transmission peak sets at the right side of E_F at low bias. With further increasing the bias, the peak becomes weak and gradually moves to high energy region. So the NDR behavior presents at a relative wide range of bias voltage. At the same time, we can notice that the peaks are still within the energy bias window(EVB) with increasing the bias, indicating a good metallic characteristic of spin-up current in P configuration. However, the spin-down transmission spectra almost vanished within the EVB as shown in Fig. 6(b), leading to a perfect spin-filtering behavior with high spin-polarization in P configuration. The spin-related transmission spectra in AP configuration were also displayed from Figs. 6(c) to 6(f). When we applied the positive bias in AP configuration, the spin-down transmission spectra peaks appear within the EVB which performed similarly to Fig. 6(a), while the spin-up transmission spectra are completely suppressed within the positive EVB. Additionally, the case is just opposite when applied the negative bias with the spin-down electrons participating in transport channels at positive bias. The interesting phenomena of perfect spin-filtering, spin-rectifying and spin-NDR behaviors were demonstrated.

These fascinating phenomena can also be elaborated by the spin resolved band structures of the left/right electrode and transmission spectra: for P configuration at the bias of 0.5 and 1.0 V in Figs. 7(a) and 7(b), and for AP configuration at the bias of ± 0.5 V in Figs. 7(c) and 7(d), respectively. From the spin-resolved band structures presented in Fig. 7, we can see that the ZGNR in the FM magnetic state display metallic behavior and spin-polarized with spin-up and spin-down bands separating from each other. As we known, when applied the positive bias, the subbands of left electrode will shift downward and those will shift upward in right electrode. One can see from Fig. 7(a), a broad and strong spin up peak appeares around the E_F for the spin-up of π^*-subband of left lead matches well with π^*-subband of right leads within the EBW, which could induce large current at the bias of 0.5 V in P configuration. The spin-down π^*-subband of left/right lead separates prominently within the EBW apart from the π^*-subband of left lead can overlap with the π-subband of the right lead. According to some researchers' study[6,14], the π^* (π)-subband of 6-ZGNR in FM state has odd (even) parity under the yz

midplane mirror operation. Since the symmetry of electron transport channels of two subbands is completely opposite, the spin-down transmission spectra within the EBW are gravely suppressed. This is the source of the large spin-filtering in P spin configuration. When the applied bias increased at 1.0 V, the overlap between the spin-up π^*-subband of left and right leads significantly decrease within a large EBW in Fig. 6(b) indicating a NDR behavior. Moreover, only the spin-up π^*-subband of left/right electrode can align with each other within the EBW, which resulted in a single spin-conducting in P configuration. While for AP configuration, the spin-related behaviors at 0.5 V in Fig. 7(c) are opposite to that in Fig. 7(a) around the E_F. The spin-down π^*-subbands of left/right electrode have big overlap within the EBW with a broad spin-down transport peak appearing at E_F, while the transport channels are completely forbidden for spin-up electrons. When applied the opposite bias, the subbands of left (right) electrode shift upward (downward). The spin-up π^*-subbands of left and right electrode are matched well within the EBW, leading to strong peak appeared around the E_F. While the spin-down of π-subband of left lead can only overlap with the spin-down π^*-subband of right lead within the EBW, the transport channels are also completely suppressed for the asymmetric parity of two subbands. We can reach a conclusion that a perfect spin-polarization with 100% SFE can be obtained with a metallic behavior of one kind spin electron and a completely suppressed of another.

4 Conclusions

We investigated the atomic structure and spin transport properties of a chromium porphyrin molecular attached to two semi-infinite ferromagnetic 6-ZGNR electrodes by performing NEGF in combination with the DFT method. The separation of spin-resolved LDOS at the Fermi level revealed that our proposed molecular device can be spin-filtering with 100% spin-polarization at zero bias in P and AP configuration. Moreover, the perfect spin polarized currents with large magnitude of SFE can be obtained by changing the orientation of external magnetic fields. Furthermore, a large spin-rectification ratio can reach to 10^4 in AP configuration and the obvious spin NDR effects can be observed in our proposed molecular device. These interesting spin-related phenomena can be understood via presenting the separation of spin-resolved LDOS, the distributions of the HOMO and LUMO and the spin transmission spectra combined with band structures of electrodes at different bias. All in all, the designed molecular device reveals a great potential usage in multiple-effect spintronics devices.

Acknowledgments

This work was supported by the National Natural Science Foundation of China (Grant Nos. 11074069, 61176116), the Specialized Research Fund for the Doctoral Program of Higher Education of China (Grant No. 20120161130003).

References

1 M. Di Ventra, S. T. Pantelides and N. D. Lang, *Phys. Rev. Lett.*, 2000, **84**, 979–982.
2 N. J. Tao, *Nat Nano*, 2006, **1**, 173–181.
3 A. J. Kronemeijer, H. B. Akkerman, T. Kudernac, B. J. van Wees, B. L. Feringa, P. W. M. Blom and B. de Boer, *Adv. Mater*, 2008, **20**, 1467–1473.
4 J. R. Petta, S. K. Slater and D. C. Ralph, *Phys. Rev. Lett.*, 2004, **93**, 136601.
5 A. R. Rocha, V. M. Garcia-suarez, S. W. Bailey, C. J. Lambert, J. Ferrer and S. Sanvito, *Nat. Mater*, 2005, **4**, 335–339.
6 Z. Li, H. Qian, J. Wu, B.-L. Gu and W. Duan, *Phys. Rev. Lett.*, 2008, **100**, 206802.
7 X. F. Yang, Y. S. Liu, J. F. Feng, X. F. Wang, C. W. Zhang and F. Chi, *J. Appl. Phys.*, 2014, **116**, 124312.
8 A. Aharony, O. Entin Wohlman, Y. Tokura and S. Katsumoto, *Phys. Rev. B*, 2008, **78**, 125328.
9 H. Wan, B. Zhou, X. Chen, C. Q. Sun and G. Zhou, *J. Phys. Chem. C*, 2011, **116**, 2570–2574.
10 Y. S. Liu, X. F. Wang and F. Chi, *J. Phys. Chem. C*, 2013, **1**, 8046–8051.
11 T. Chen, X. F. Li, L. L. Wang, K. W. Luo, Q. Li, X. H. Zhang and X. J. Shang, *EPL (Europhysics Letters)*, 2014, **105**, 57003.
12 J. J. Zhang, Z. H. Zhang, J. Li, D. Wang, Z. Zhu, G. P. Tang, X. Q. Deng and Z. Q. Fan, *Org. Electron.*, 2014, **15**, 65–70.
13 A. Staykov, D. Nozaki and K. Yoshizawa, *J. Phys. Chem. C*, 2007, **111**, 11699–11705.
14 J. Zeng, K. Q. Chen, J. He, X. J. Zhang and C. Q. Sun, *J. Phys. Chem. C*, 2011, **115**, 25072–25076.
15 R. Pati, L. Senapati, P. M. Ajayan and S. K. Nayak, *Phys. Rev. B*, 2003, **68**, 100407.
16 M. Urdampilleta, S. Klyatskaya, J. P. Cleuziou, M. Ruben and W. Wernsdorfer, *Nat. Mater*, 2011, **10**, 502–506.
17 H. Hao, X. Zheng, L. Song, R. Wang and Z. Zeng, *Phys. Rev. Lett.*, 2012, **108**, 017202.
18 A. N. Pasupathy, R. C. Bialczak, J. Martinek, J. E. Grose, L. A. K. Donev, P. L. McEuen and D. C. Ralph, *Science*, 2004, **306**, 86–89.
19 P. Zhao, Q. H. Wu, D. S. Liu and G. Chen, *J. Chem. Phys.*, 2014, **140**, 044311.
20 J. Huang, W. Wang, Q. Li and J. Yang, *J. Chem. Phys.*, 2014, **140**, 164703.
21 Y. Ni, K. l. Yao, C. q. Tang, G. y. Gao, H. h. Fu and S. c. Zhu, *RSC Advances*, 2014, **4**, 18522–18528.
22 J. Miguel, C. F. Hermanns, M. Bernien, A. Krüger and W. Kuch, *J. Phys. Chem. Lett.*, 2011, **2**, 1455–1459.
23 W. J. Cho, Y. Cho, S. K. Min, W. Y. Kim and K. S. Kim, *J. Am. Chem. Soc.*, 2011, **133**, 9364–9369.
24 H. S. Kang and Y.-S. Kim, *J. Phys. Chem. C*, 2012, **116**, 8167–8173.
25 J. Zeng and K. Q. Chen, *J. Mater. Chem. C*, 2013, **1**, 4014–4019.
26 Y. Chen, A. Prociuk, T. Perrine and B. D. Dunietz, *Phys. Rev. B*, 2006, **74**, 245320.
27 A. K. Geim and K. S. Novoselov, *Nat. Mater*, 2007, **6**, 183–191.
28 X. Li, X. Wang, L. Zhang, S. Lee and H. Dai, *Science*, 2008, **319**, 1229–1232.
29 K. S. Novoselov, A. K. Geim, S. V. Morozov, D. Jiang, Y. Zhang, S. V. Dubonos, I. V. Grigorieva and A. A. Firsov, *Science*, 2004, **306**, 666–669.
30 O. V. Yazyev and M. I. Katsnelson, *Phys. Rev. Lett.*, 2008, **100**, 047209.
31 M.-Q. Long, L. Tang, D. Wang, L. Wang and Z. Shuai, *Journal of the American Chemical Society*, 2009, **131**, 17728–17729.
32 W. Han and R. K. Kawakami, *Phys. Rev. Lett.*, 2011, **107**, 047207.

33 B. Larade, J. Taylor, H. Mehrez and H. Guo, *Phys. Rev. B*, 2001, **64**, 075420.

34 C. Jin, H. Lan, L. Peng, K. Suenaga and S. Iijima, *Phys. Rev. Lett.*, 2009, **102**, 205501.

35 R. N. Wang, X. H. Zheng, J. Lan, X. Q. Shi and Z. Zeng, *RSC Advances*, 2014, **4**, 9172–9177.

36 Y. Liu, X. Zhang, J. Feng and X. Wang, *Appl. Phys. Lett.*, 2014, **104**, 242412.

37 M. G. Zeng, L. Shen, Y. Q. Cai, Z. D. Sha and Y. P. Feng, *Appl. Phys. Lett.*, 2010, **96**, 042104.

38 F. Prins, A. Barreiro, J. W. Ruitenberg, J. S. Seldenthuis, N. Aliaga-Alcalde, L. M. K. Vandersypen and H. S. J. van der Zant, *Nano Letters*, 2011, **11**, 4607–4611.

39 C. A. Reed, J. K. Kouba, C. J. Grimes and S. K. Cheung, *Inorg. Chem.*, 1978, **17**, 2666C2670.

40 D. M. Guldi, P. Neta and P. Hambright, *J. Chem. Soc., Faraday Trans.*, 1992, **88**, 2013–2019.

41 Y. W. Son, M. L. Cohen and S. G. Louie, *Nature*, 2006, **444**, 347–349.

42 W. Y. Kim and K. S. Kim, *Nat. Nano*, 2008, **3**, 408–412.

43 T. Ozaki, K. Nishio, H. Weng and H. Kino, *Phys. Rev. B*, 2010, **81**, 075422.

44 M. Brandbyge, J.-L. Mozos, P. Ordejón, J. Taylor and K. Stokbro, *Phys. Rev. B*, 2002, **65**, 165401.

45 J. P. Perdew, K. Burke and M. Ernzerhof, *Phys. Rev. Lett.*, 1996, **77**, 3865–3868.

46 M. Büttiker, Y. Imry, R. Landauer and S. Pinhas, *Phys. Rev. B*, 1985, **31**, 6207–6215.

47 J. Chen, M. A. Reed, A. M. Rawlett and J. M. Tour, *Science*, 1999, **286**, 1550–1552.